In situ exsolution of Ni particles on the PrBaMn2O5 SOFC electrode material monitored by high temperature neutron powder diffraction under hydrogen

M. Bahout, P.B. Managutti, V. Dorcet, A. Le Gal La Salle, Serge Paofai, T.C. Hansen

In situ exsolution of Ni particles on the PrBaMn$_2$O$_5$ SOFC electrode material monitored by high temperature neutron powder diffraction under hydrogen

Mona Bahout[1], Praveen Managutti[1], Vincent Dorcet[1], Annie Le Gal La Salle[2], Serge Paofai[1] and Thomas Hansen[3]

[1]Univ Rennes, CNRS, Institut des Sciences Chimiques de Rennes-UMR6226-ScanMAT-UMS2001, 263 Avenue du Général Leclerc, 35042 Rennes, France
[2]Institut des Matériaux Jean Rouxel (IMN), CNRS UMR 6502, Université de Nantes, 2 rue de la Houssinière, B.P. 32229 Nantes Cedex 3, France
[3]nstitut Laue-Langevin, 1 avenue des Martyrs CS 20156, 38042 Grenoble Cedex 9, France

Abstract

NiO has been incorporated into the nominal perovskite composition Pr$_{0.5}$Ba$_{0.5}$MnO$_{3-\delta}$ to produce, upon heating under hydrogen atmosphere, *in situ* exsolved Ni-catalyst supported onto the PrBaMn$_2$O$_5$ anode material. Transmission electron microscopy (TEM) and neutron powder diffraction (NPD) showed that initial composition obtained by annealing in air at 950 °C consists of two perovskite phases; orthorhombic Pr$_{0.65}$Ba$_{0.35}$Mn$_{0.975}$Ni$_{0.025}$O$_3$ (S.G. *Ibmm*, ~ 75 wt. %) and 2H-hexagonal BaMnO$_{3-\delta}$ (S.G. *P6$_3$/mcm,* 25 wt %). On heating the two-phase sample under wet hydrogen, MnO particles exsolve at *T* ~ 500 °C meanwhile the orthorhombic phase transforms to tetragonal (S.G. *I*4/*mcm*) then to cubic (S.G. *Pm-3m*) at *T* ~ 665 °C. When the temperature approaches 900 °C, the emergence of Ni metal particles was detected in the neutron diffraction patterns while the two perovskite phases were transforming into a Ni-free layered double perovskite, PrBaMn$_2$O$_{5(1)}$. *In situ* real time observation of the structural changes under hydrogen in the 800-900 °C temperature range provided evidence of the simultaneity of Ni exsolution and phase transformation within our timescale resolution. From quantitative Rietveld analysis, the fraction of exsolved nickel represents the whole amount of Ni introduced in the synthesis of the as-prepared PBMN material. Impedance spectroscopy measurements in 5% H$_2$ atmosphere show promising electrochemical performance for the Ni-

exsolved layered perovskite electrode with a polarization resistance of 0.4 Ω cm^2 at 800 °C (0.135 Ω cm^2 at 850 °C) without any optimization.

Keywords:

SOFC anode; Ni exsolution; layered perovskite manganite; solid oxide fuel cells, nanoparticles, *in situ* neutron diffraction, nanocatalyst.

1. Introduction

Solid oxide fuel cells (SOFCs) which transform chemical energy to electrical energy by an electrochemical conversion process with high efficiency and less CO_2 emission in comparison to most other conventional power generation systems are considered among the cleanest promising technologies to generate electricity[1-3]. Conventional SOFCs employ Ni-based cermet anodes which display high electronic conductivity, excellent electrocatalytic activity for fuel oxidation and good compatibility with zirconia- or ceria-based electrolytes but suffers from serious drawbacks such as volume change on redox cycling and Ni coarsening during operation as well as carbon build-up (coking) and sulfur contamination from hydrocarbon fuels[4-6]. Several materials have been investigated as alternatives to Ni-based cermet anode to overcome coking and impurity poisoning issues and *A*-site layered double perovskites (LDP) LnBaMn$_2$O$_{5+\delta}$ (Ln = Pr, Nd) have received particular attention owing to their mixed ionic and electronic conductivity (MIEC), redox stability, superior resistance to coking and sulfur poisoning and good mechanical compatibility with common electrolytes but their (electro)catalytic activity for fuel oxidation is insufficient for practical applications[7-11]. Recently, exsolution of metal nanoparticles from a host oxide lattice has emerged as a promising catalyst design to improve the electrode performance and stability in replacement

to the infiltration and impregnation technique[12-16]. Some potential drawbacks of these methods include non-uniform distribution of the nanoparticles, reduced porosity of the electrode and complicated processing procedures[17] as well as coarsening of the nanoparticles at elevated temperature[18]. In exsolution, (electro)catalytic elements are introduced in the crystal lattice during the synthesis in oxidizing conditions forming a solid solution and precipitate (exsolve) on the surface of the oxide phase as uniformly dispersed metal nanoparticles (NPs) upon heating the sample in hydrogen at $T \geq 800$ °C. Pd-, Pt- and Rh-exsolved $LaFeO_3$ perovskite are well-known catalysts for automotive emission control[19]. Unlike the conventional impregnation method, *in situ* exsolution delivers thermally stable and uniformly dispersed NPs[20-26]. Particularly, the *A*-site deficiency in perovskites giving the stoichiometry $A_{1-\alpha}BO_{3-\delta}$ promotes exsolution of the reducible *B* cations[27-30]. Indeed, perovskite manganites are known to develop *A*-site overstoichiometric surfaces and therefore *A*-site deficient formulations are used to minimize *A*-site cation segregation[31,32] which is detrimental to exsolution[29].

A few years ago, we published the first real time *in situ* high temperature neutron powder diffraction (NPD) of the layered double perovskite (LDP) manganite, $NdBaMn_2O_{5+\delta}$, under hydrogen atmosphere[8,9]. In the work reported here, we target the synthesis of Ni-doped *A*-site deficient LDP manganite, $(LnBa)_{1-x/2}Mn_{2-x}Ni_xO_{5+\delta}$ with Ln = Pr and x = 0.05. In addition to being a good model system, this composition is representative of a range of oxides that have been shown to be active for metal and metal alloys exsolution (Mn, Co, Ni, Fe, FeCo) and suitable as electrodes in solid oxide electrochemical cells[33,34].

A-site deficiency has not been investigated in LDP manganites so far. In our formulations, the *A*-site deficiency and correlated Ni-content have been chosen such that the LDP composition approaches stoichiometry upon total Ni exsolution, according to the reaction:

$$(Ln\text{Ba})_{1-x/2}\text{Mn}_{2-x}\text{Ni}_x\text{O}_5 \quad \rightarrow \quad (1-x/2)\ Ln\text{BaMn}_2\text{O}_5 + x\ \text{Ni}$$
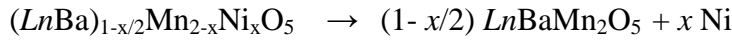
Modest Ni^{2+} doping levels ($x = 0.05$) have been used due to low solubility of Ni in the host lattice. We used high temperature *in situ* neutron powder diffraction (NPD) under hydrogen (5% H_2/He) and Rietveld phase analysis to monitor Ni particle exsolution and investigate the underlying structural evolution. To date the characterization of the exsolution process has been performed mostly in *ex situ* conditions by X-ray diffraction (XRD), scanning and transmission electron microscopy (SEM/TEM), atomic force microscopy and X-ray photoelectron spectrometry (XPS)[35,36]. An *in situ* study reports on atomic-scale visualization of Co NPs exsolution on the $\text{PrBaMn}_{1.8}\text{Co}_{0.2}\text{O}_5$ double perovskite using an environmental transmission electron microscope[34]. For the whole perovskite family, *in situ* characterization of the exsolution phenomena by neutron diffraction techniques is unavailable. This work aims to respond to this lack of information by detailed high temperature neutron powder diffraction study of nickel exsolution in double perovskite manganites [30,37,38].

2. Experimental

Polycrystalline powder of $(\text{PrBa})_{1-x/2}\text{Mn}_{2-x}\text{Ni}_x\text{O}_{6-\delta}$ with $x = 0.05$ was prepared using a citrate-nitrate sol-gel route. Stoichiometric amounts of nitrates metal precursors, $\text{Pr(NO}_3)_3.6\text{H}_2\text{O}$ (Aldrich, 99.9%), $\text{Ba(NO}_3)_2$ (Aldrich, 99%), $\text{Mn(NO}_3)_2.4\text{H}_2\text{O}$ (Aldrich, 98%), $\text{Ni(NO}_3)_2.6\text{H}_2\text{O}$

(Aldrich, 98.5 %) were dissolved in distilled water under continuous stirring and heating ($T \sim$ 40 °C) then citric acid (CA) (Acros Organic, 99 %) and ethylene glycol (EG) (Sigma-Aldrich) were introduced. The molar ratio of EG/CA/total metal ions was around 3:1.5:1. The pH value was adjusted at $\sim$ 8 with ammonia (NH_4OH 28 vol. %) to avoid precipitation of the cations. The temperature was increased to $T \sim$ 180 °C and the solution was kept stirring and heating until a resin containing homogeneously distributed cations forms and autoignition occurred. The product was calcined at $T \sim$ 600 °C overnight to decompose most of the organic components. The resulting ash-like precursor was ground in an agate mortar, pressed into pellets (2 mm thick, 13 mm diameter) and heated at $T \sim$ 950 °C for 24 h in a muffle furnace then cooled to room temperature (RT) at a rate of $\sim$ 4 °C min^{-1}. This sample, hereafter called "as-prepared PBMN-5", was used for the NPD and DSC (differential scanning calorimetry) experiments. In order to examine the behavior of as-prepared PBMN-5 in hydrogen atmosphere, simultaneous thermal gravimetric (TGA) and DSC analyses were carried out on a Netzsch (STA 449F3) instrument. The sample was heated under dry 5% H_2/N_2 (40 mL min^{-1}) from 20 to 1000 °C and subsequently cooled (heating/cooling rate of 20 °C min^{-1}). Transmission Electron Microscopy (TEM) was performed using a JEOL JEM-2100 LaB$_6$ Transmission Electron Microscope operating at 200 kV and equipped with an Oxford Silicon Drift Detectors (SSD) X-Max^{N} 80T for Energy Dispersive X-ray Scattering (EDS) measurements. The sample was crushed in dry ethanol and a drop of the suspension was deposited on a carbon-coated film (copper grid).

Temperature-dependent neutron powder diffraction experiments were carried out in the temperature range 20-900 °C on the high-flux two-axis D20 neutron diffractometer at the high-flux reactor of the Institut Laue-Langevin (ILL, Grenoble, France)[39]. The set-up is the

same as that described previously[40]. A take-off angle of 90 ° from the (115) plane of a germanium monochromator was chosen, giving a wavelength of $\lambda \sim 1.54$ Å and a resolution of $\Delta d/d \sim 2.9 \times 10^{-3}$, while retaining a high flux on the sample ($\sim 1.6 \times 10^7$ n cm^2 s^{-1}). A sample of ~ 4.5 g was loaded at the centre of a quartz tube (8 mm inner diameter). Two K-type thermocouples were placed in the quartz tube; one a few mm above the sample to monitor the temperature and another below the sample to adjust the temperature. The temperature was programmed to increase linearly at 10 °C min^{-1} from 20 to 300 °C and at 2 °C min^{-1} from 300 °C to 900 °C and subsequent cooling. The data were summed, and the counters were reset to zero every 600 s, thus giving a temperature resolution of 50 and 20 °C, respectively. Besides the data collected on ramping, few isothermal data sets were recorded at relevant temperatures; 300 (6 × 10 min), 800 (4 × 30 min) and 900 °C (4 × 30 min) as well as in the beginning and the end of the reducing cycle. The temperature profile used under wet 5% H$_2$/He flow for the as-prepared PBMN-PBMN sample is displayed in Fig. S.I.1.

The diffraction patterns were analyzed by the Rietveld method[41,42] using the program FullProf and its graphic interface WinPLOTR[43]. The background was modelled using linear interpolation between $\sim$ 60 points and two asymmetry parameters were refined below 2θ = 55°. The unit cell parameters and zero-point shift were refined. The peak profile was modeled using a Thompson-Cox-Hastings pseudo-Voigt profile function[44]. The atomic coordinates, the oxygen occupancy and the isotropic displacement parameters (B_{iso}) of all the atoms were refined.

To check the catalytic effect of the exsolved nanoparticles towards H$_2$ oxidation, electrochemical impedance spectroscopy (EIS) measurements were realized on symmetric cells under 5% H$_2$/Ar flow in the temperature range 850-650 °C. Two compositions were

studied; reduced (*i.e*. Ni-exsolved) and reduced $PrBaMn_2O_5$ (PBM) used for comparison. The inks were prepared by mixing 60 wt % of the powder sample with 40 wt % of α-terpineol (99% Acros Organics) /ethyl cellulose (Aldrich) (95/5 w/w) mixture. Dense 8YSZ (8% yttria-stabilised zirconia TOSOH) discs were used as the electrolyte. Due to the reactivity of the electrode materials with the 8YSZ electrolyte, a $Ce_{0.9}Gd_{0.1}O_{1.95}$ (CGO)[10,45] buffer layer (500 nm) was deposited by physical vapor deposition on both sides of the electrolyte. The electrode ink was deposited on both sides of the electrolyte followed by sintering in air at 1100 °C for 3h. The current collectors consist of gold grid discs ($A = 0.95$ cm^2) connected to the electrodes and linked to the external current and voltage circuits. The discs were placed into the open-flange setup^{TM} provided by the Swiss company Fiaxell as described previously[46]. It contains an oven and an Inconel 600 & 601 support in order to maintain the cell in the furnace. EIS was performed in potentiostatic mode using a VersaSTAT device and associated VersaStudio software in the 0.1-10,000 Hz frequency range at open circuit voltage (OCV) conditions with an AC signal amplitude of 20 mV or 10 mV; the amplitude value was optimized for each measurement in order to get the best signal to noise ratio without loss of the transfer function linearity.

The cells were heated in air at 2 °C min^{-1} up to $T \sim 600$ °C then fed with a 5% H_2/Ar gas mixture at a flow rate of 200 mL min^{-1} and the temperature was increased to 850 °C. Before starting the measurements, the samples were stabilized at $T \sim 850$ °C until no variation of the impedance spectra was observed (24h). Data were collected on cooling from 850 to 600 °C at 50 °C intervals with a stabilization time of 4h at each temperature. The impedance diagrams were analysed using the ZView® software (D. Johnson, *ZView: A software program for IES analysis, Version 2.8,* Scribner associates, INC, Southern Pines, NC, 2002).

Preliminary analysis of the product

The crystalline structure of 5 before reduction was examined by powder X-ray diffraction (XRD) are consistent with the existence of a cubic perovskite and a hexagonal perovskite structures without any secondary phases. Electron diffraction analysis of the cubic perovskite shows weak superstructure reflections (Figs. 2a and b, see arrows) related to octahedral tilting consistent with a ($a\sqrt{2} \times a\sqrt{2} \times 2a$) supercell and the *Ibmm* space group as reported for $Pr_{0.7}Ba_{0.3}MnO_3$[47]. Figure 2c displays a typical SAED pattern of a hexagonal perovskite crystallite oriented along the $[\bar{1}10]$ zone axis. The structure is mainly two-layer (2H) with the lattice parameters, $a \approx 5.7$ Å and $c \approx 4.8$ Å (space group $P6_3/mmc$) consistent with the XRD data. The presence of streaks along the $c*$ direction can be attributed to disordered stacking faults as described by Parras *et al.*[32]. TEM-EDS analysis shows the orthorhombic and hexagonal perovskite compositions to be close to $Pr_{0.65(3)}Ba_{0.35(3)}Mn_{0.97(1)}Ni_{0.03(1)}O_3$ and $BaMnO_3$, respectively (Fig. S.I. 1).
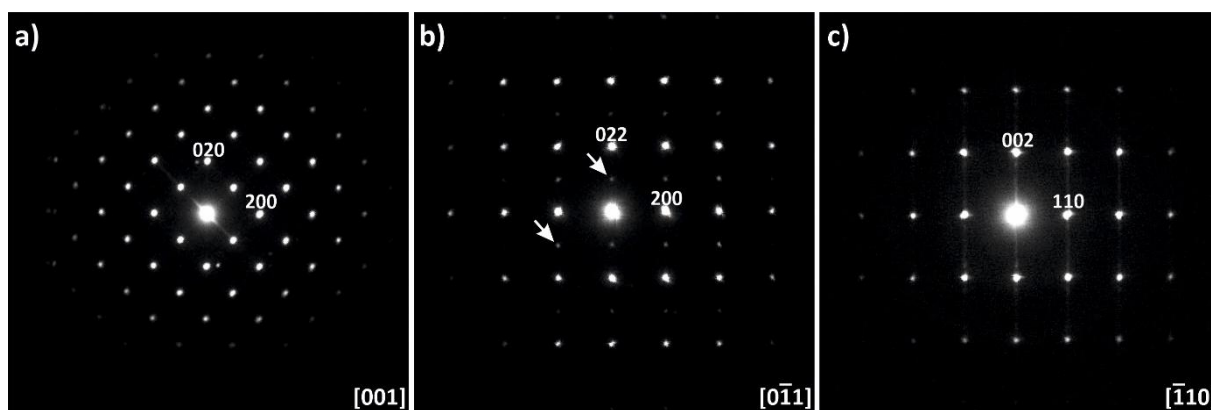
Fig. 2. SAED of as-prepared PBMN: zone axis pattern (a) [001] and (b) $[0\bar{1}1]$ of an orthorhombic *Ibmm* perovskite crystallite and (c) $[\bar{1}10]$ of a hexagonal perovskite crystallite.

As-prepared PBMN was heated under 5% H_2/Ar at $T \sim 900$ °C for 18 h to produce the layered perovskite manganite. TEM-EDS analysis of few tens of "particles" showed the existence of

two phases: a Ni-free $PrBaMn_2O_x$ phase (Fig. S.I. 3) and Ni particles/clusters of ~ 80 nm diameter (Fig. 3). These analyses carried out on a large number of particles indicate that Ni has been completely exsolved from the perovskite structure.
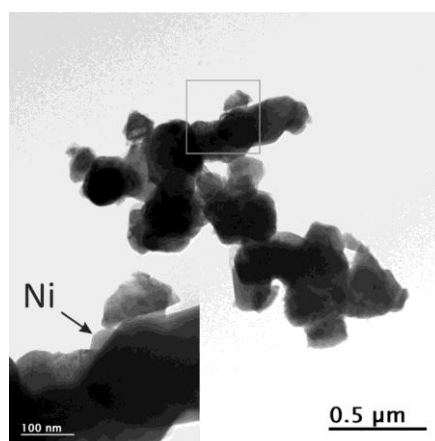

Fig. 3. Bright field TEM image of reduced PBMN. The grey square area is enlarged highlighting Ni exsolved particle.

The results of thermal analysis, displayed in Fig. S.I. 4, indicate on the DSC curve two transitions on heating at T ~ 450 and ~ 900 °C and, one transition on cooling at T ~ 525 °C. The TGA (Thermogravimetric analysis) curve shows a rapid mass decrease between 400 °C and 500 °C on heating, consistent with the DSC signal observed at T ~ 450 °C and subsequent smoother mass loss up to 800 °C due to diffusion phenomenon. The temperature range of this mass variation is consistent with that reported for $Pr_{0.5}Ba_{0.5}MnO_{3-\delta}$ assigned to the phase transformation from simple to double perovskite[11]. However, as shown in the neutron section, our material has not transformed yet to a layered perovskite in this temperature range. Moreover, the mass variation of ~ 3 wt. % involved at this stage cannot be assumed to oxygen loss only (in such as case it would correspond to a perovskite with 2.55 oxygen/f.u. inconsistent with the oxygen content refined form NPD) but may also include dehydration or

removal of adsorbed water. When the temperature exceeds 800 °C, a second weight loss concomitant with the presence of the small exothermic peak at $T \sim 900$ °C on the DSC curve proceeds and completes with the increase in temperature. By comparing the reducibility of the elements, it can be speculated that this weight loss of ~ 0.7 wt. % corresponds to the removal of oxygen atoms bonding Ni^{2+} and the reduction of Ni^{2+} to metallic Ni while the material transforms to a layered perovskite, as demonstrated by *in situ* NPD.

3. Neutron diffraction

Figure 5 displays the Rietveld analysis of the neutron powder diffraction data collected at $T \sim 60$ °C prior to reduction. The as-prepared PBMN sample consists of two perovskites; an orthorhombic phase (space group *Ibmm* # 74, $a = 5.5079$ (3) Å, $b = 5.4893(2)$ Å, $c = 7.7539(4)$ Å) and a two-layer $BaMnO_{3-\delta}$ hexagonal (2H) phase (space group $P6_3/mmc$ # 194, $a = 5.6869(2)$ Å, $c = 4.7916(3)$ Å) . No NiO secondary phase (space group *Fm-3m*, $a = 4.176$ Å) was detected.
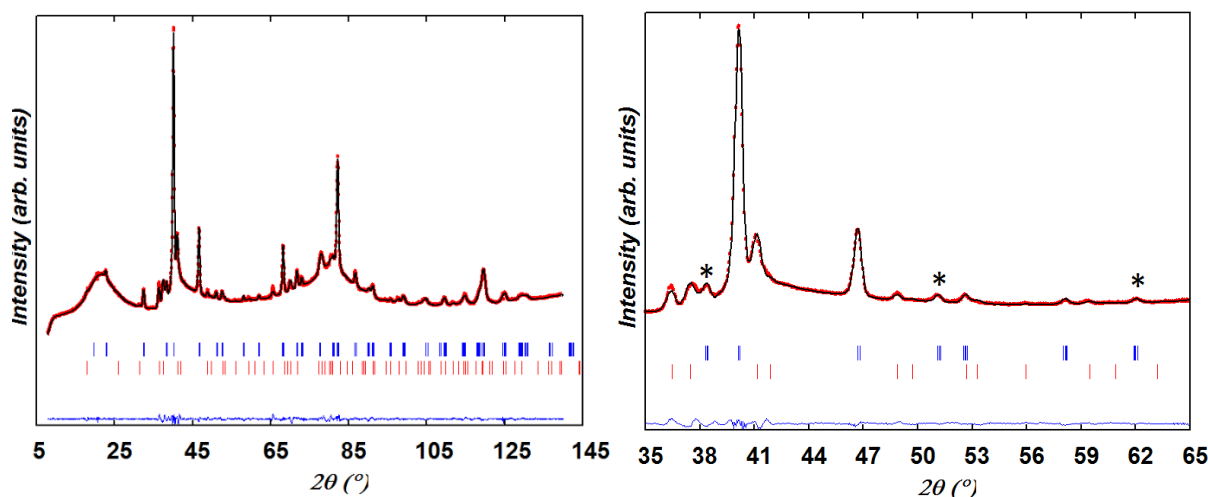
Fig. 4. Observed, calculated, and difference neutron powder diffraction patterns for as-prepared PBMN at $T \sim 60$ °C. Tick marks indicate the reflection positions for (upper) $(Pr,Ba)MnO_{3-\delta}$ (S.G. *Ibmm*) and (lower) 2H-$BaMnO_{3-\delta}$ (S.G. $P6_3/mmc$) perovskites. Few peaks (*) unindexed in cubic symmetry (S.G. *Pm-3m*) are emphasized.

The ratio of the Pr and Ba cations at the A site of the orthorhombic and hexagonal perovskites could not be refined due to small difference between the scattering lengths of Ba (5.07 fm) and Pr (4.58 fm)[48]. The compositions of the orthorhombic and hexagonal phases were therefore fixed at $Pr_{0.65}Ba_{0.35}Mn_{0.975}Ni_{0.025}O_3$ and $BaMnO_3$, respectively on the basis of the EDS analysis. The A-site deficiency (B-site excess) targeted in our synthesis was shown not affect the quality of the fit and was consequently neglected in the refinement. The refined oxygen occupancy at the O1 ($4e$) and O2 ($8g$) sites of the orthorhombic phase converged to 0.93(7) and 1.05(5) respectively, resulting in an oxygen composition close to stoichiometry. The refinement of the Ni content in the hexagonal perovskite converged to a negative value meaning that this phase is Ni-free, in agreement with the EDS analysis. The oxygen occupancy at the $6h$ site converged to 0.81(5) resulting in 2.4(1) oxygen/formula unit (f.u.). The two-phase model produced a good fit ($\chi^2 \sim 12$, $R_{wp} \sim 8.0$ % and $R_p \sim 9.7$ %) with weight ratio for the orthorhombic and hexagonal phases of $\sim 77(4)$ and $\sim 23(1)$ wt. %, respectively. The refined structural parameters are given in Table S.I. 1.We should mention that the X-ray diffraction patterns reported for Co-, Ni- or Fe-doped praseodymium barium perovskite manganites prepared by annealing in air at 950 °C were shown to consist of a mixture of cubic and hexagonal phases[37].

The Pr- and Ba-content of the orthorhombic and hexagonal phases within our as-prepared PBMN sample is consistent with the Goldschmidt tolerance factor (t) which evaluates the crystal structure distortion of ABO_3 perovskites. This factor is estimated from the following equation, $t = \frac{rA + rO}{\sqrt{2} \times (rB + rO)}$.

Since the ionic radius of Pr^{3+} in smaller than the Ba^{2+} one ($r_{Pr3+} = 1.18$ Å, $r_{Ba2+} = 1.61$ Å)[49], it is expected that the orthorhombic perovskite contain larger amount of Pr^{3+} cations than Ba^{2+} cations while the reverse prevails for hexagonal perovskites. Indeed, various Pr-rich manganites such as $Pr_{0.65}Ba_{0.35}MnO_3$ and $Pr_{0.7}Ba_{0.3}MnO_3$ crystallize in the orthorhombic *Ibmm* S.G. while the hexagonal perovskite manganites reported so far contain only Ba at the *A* site[48]. Other space groups were reported for $Pr_{1-x}Ba_xMnO_{3-\delta}$ perovskites annealed in air, such as *Pbnm* for the compositions with $x = 0.1$[47], 0.2[50], 0.3[50] and 0.33 [51] or tetragonal symmetry for $Pr_{0.65}Ba_{0.35}MnO_3$ at low temperature (S.G. *I4/mcm* at $T \sim 210$ K and S.G. *I4/m* at $T \sim 210$ and ~ 5 K)[50] .

Heating of the sample

The two-phase sample was heated at a fast rate (10 °C min^{-1}) to $T \sim 300$ °C since no particular changes were expected in this temperature range according to the TGA-DSC analysis and at a lower rate (2 °C min^{-1}) from $T \sim 300$ °C to $T \sim 900$ °C and subsequent cooling. When the temperature approached 400 °C, additional peaks ascribed to MnO (S.G. *Fm-3m*) were observed at $2\theta \sim 34.7$ ° and ~ 70 ° in the NPD pattern. Moreover, at $T \geq 400$ °C the oxygen occupancy at the O1 site in the body-centered phase starts decreasing while the amount of MnO increases. The Rietveld plot for the data collected at $T \sim 510$ °C is shown in Fig. S.I. 5. No significant changes were detected on heating from 500 to $T \sim 665$ °C besides the decrease of the orthorhombic distortion of the *Ibmm* phase whose *a* and *b* lattice parameters become closer, as illustrated in Fig. 5. The percentages of the body-centered and hexagonal phases remain unchanged as well as their oxygen content, respectively close to 2.7 and 2.5 atoms/formula unit (f.u.)
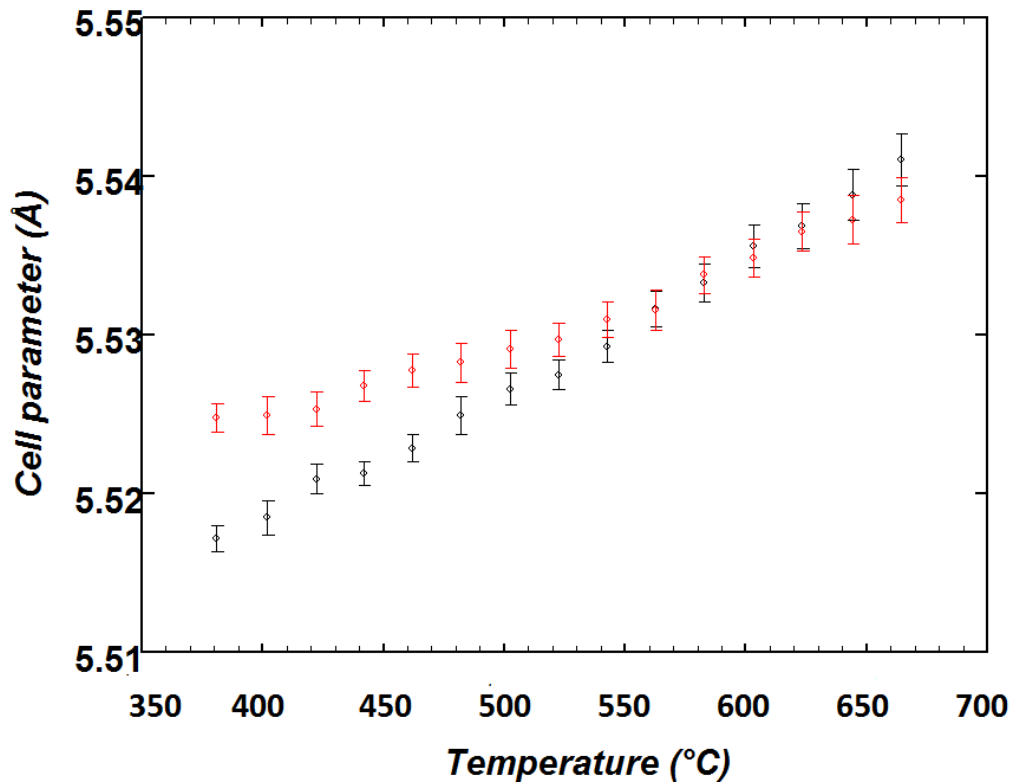
Fig. 5. Evolution of the (red) a and (black) b lattice parameters of (Pr,Ba)MnO$_{3-\delta}$ perovskite (S.G. *Ibmm*) on heating as-prepared PBMN under wet 5% H$_2$/He.

At $T \geq 510$ °C, the multi-phase refinement using the tetragonal space group $I4/mcm$ gave similar goodness-of-fit indicators to the orthorhombic *Ibmm* one and therefore the former was used to model the body-centered phase.

When the temperature reached 665 °C, small peaks arising from a cubic perovskite phase (S.G. *Pm-3m*) whose composition was shown to be the same as the tetragonal one were detected. Therefore, sequential refinements accounting for the coexistence of three perovskite phases (tetragonal, cubic and hexagonal) as well as MnO were therefore undertaken up to $T \sim$ 800 °C. To avoid instability in the multiphase refinements, B_{ov} was refined for each phase

instead of B_{iso} of the individual atoms. Fig. 6 displays the evolution of the phase fractions of the tetragonal and cubic perovskites in the temperature range 665- 800 °C.
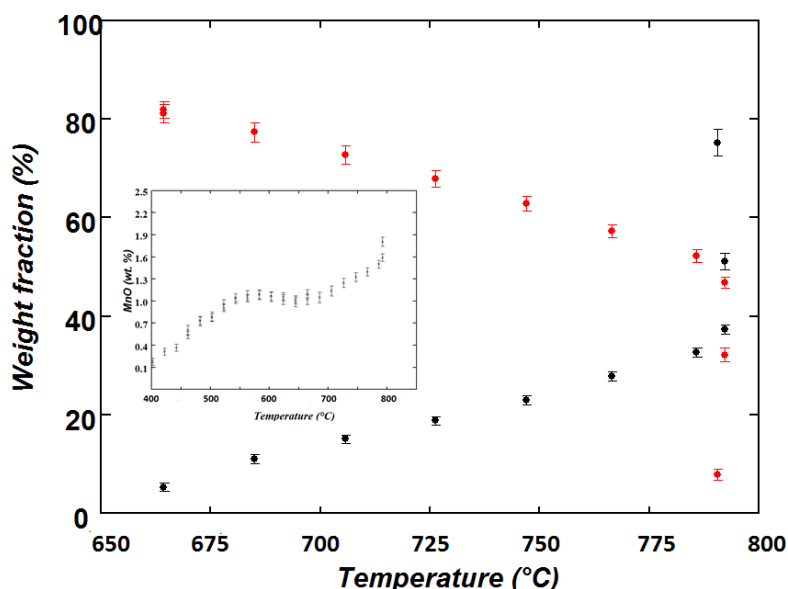
Fig. 6. Evolution of the weight fractions on heating as-prepared PBMN under 5% H_2/He; (red) in the temperature range 665-800 °C; (red) body-centered perovskite, (black) cubic perovskite. Insight shows the weight fraction evolution of MnO in the temperature range 400-800 °C.

After 2 h of isothermal heating at a temperature close to 800 °C the tetragonal perovskite has completely transformed into a cubic one. During this phase transition, the amount of the hexagonal phase remains constant (~ 15 wt. %) as well as its oxygen content (2.5 atoms/f.u.) and the oxygen content of the cubic perovskite (~ 2.7(1) atoms/f.u). while the quantity of MnO has increased. The profile of two representative patterns collected during this transition is shown in Fig. S.I. 6. After 2 h of heating at 800 °C, the temperature was increased at 2°C min^{-1} to 900 °C and the sample was held 2h at T ~ 900 °C at which four datasets were collected at 30 min intervals. Fig. 7 displaying relevant curves recorded throughout this heating ramp show that an additional peak at 2θ ~ 44 ° ascribed to Ni is detected at T = 870 °C and that its intensity increases on heating. At the same time, the contribution of the

hexagonal perovskite decreases, as revealed by the decrease of characteristic peaks (labelled *
in Fig. 7) at $2\theta \sim 27, 38, 41°$ while a layered perovskite phase emerges as seen from the
growth of a peak at $2\theta \sim 39 °$ (Fig. S.I. 7) and the presence of the (101) and (103) peaks at $T =$
900 °C (Fig. 7).
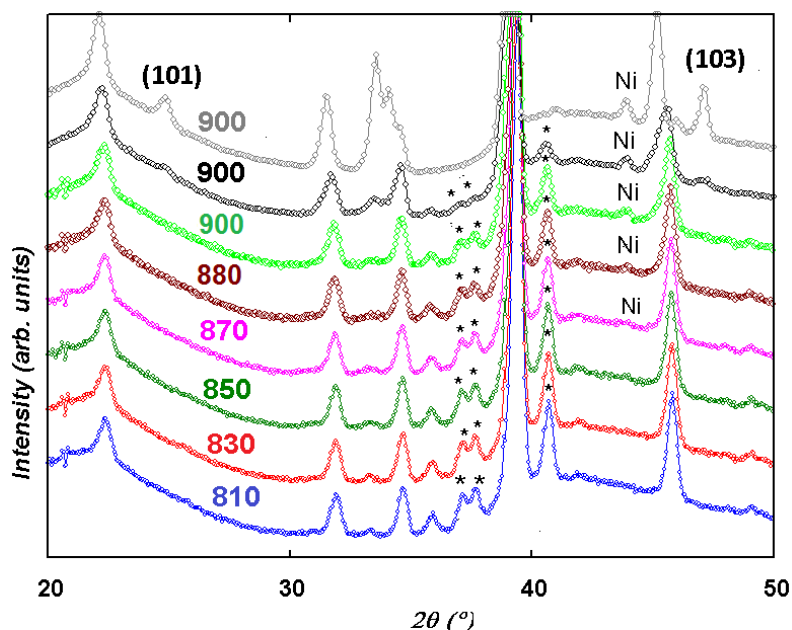
**Fig. 7. Relevant patterns collected on heating with the average temperature indicated; time
increases upwards. Simultaneous Ni exsolution and layered perovskite formation processes are
revealed by increase of the intensity of the Ni peak and decrease of the intensity of the peaks
from the hexagonal perovskite labelled (*). The (101) and (103) peaks of the layered perovskite
are shown on the last pattern at 900 °C.**

The isothermal datasets collected at 900 °C reveal large structural transformations. The first
two (Fig. 7, green and black) were modelled with 3 main phases; cubic, hexagonal and
layered perovskites in addition to MnO and Ni (Fig. S.I. 7). The two subsequent isothermal
datasets were similar (only one in grey is shown in Fig. 7) and could be modelled with
$PrBaMn_2O_5$ layered perovskite, MnO, and Ni (Fig. S.I. 8, Table S.I. 2). Both Fig. 7 and Table
S.I. 3 that lists the phase fractions in the 800-900 °C temperature range highlight that Ni
exsolution and double perovskite formation occur simultaneously within the timescale of our

experiment and completed after 60 min heating at 900 °C. Consequently, Ni exsolution does not proceed by intracrystalline diffusion of the Ni^{2+} ions from the double perovskite backbone as reported previously[34,37]. The unmixing of Ni ions with Mn at the *B*-site of the double perovskite within this experiment is consistent with the lack of layered double perovskite nickelates $LnBaNi_2O_{5+\delta}$ (*Ln* = rare earth) or mangano-nickelates, $LnBaM_{2-x}Ni_xO_{5+\delta}$. However, few layered double perovskites with little amount of Ni ions at the *B*-site along with either Co or Fe have been reported[52]. Fig. 8 summarizes the main structural changes undergone by as-prepared PBMN heated in wet 5% H_2/He atmosphere.
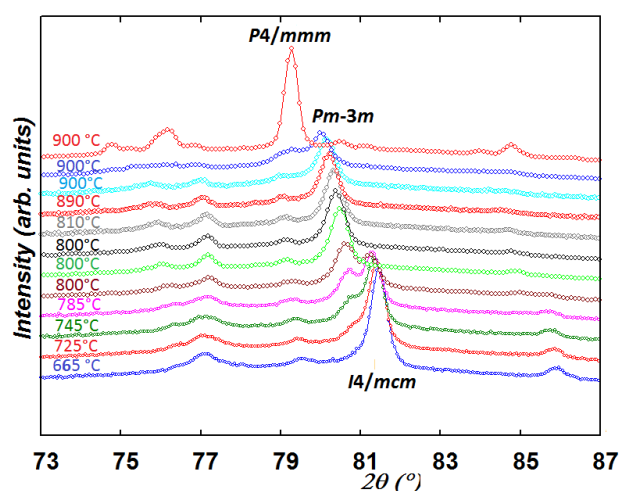
Fig. 8. *In situ* **NPD data highlighting the structural transformation of as-prepared PBMN heated under wet 5% H_2/He.**

We can stress that the onset temperature of the double perovskite construction concomitant with Ni particle formation is consistent with the mass oxygen loss and exothermic peak detected at $T \sim 870$ °C on the TGA-DSC curves (Fig. S.I.4.). This temperature is different from that reported at $T \sim 400$ °C by Sengodan *et al.*[11]. According to our results, the DSC peak at $T \sim 400$ °C corresponds to the onset of MnO exsolution from as-prepared PBMN.

Cooling from 900 °C to room temperature

The sample was cooled under wet hydrogen at a rate of 2 °C min^{-1} and the structure of the double perovskite was refined in the space group $P4/mmm$. The space group changes to $P4/nmm$ at $T \sim 550$ °C due to Mn^{3+} and Mn^{2+} charge ordering in agreement with previous results[9]. Fig. 9 which displays the Rietveld fit at $T \sim 60$ °C (lowest temperature reached on cooling) and Table S.I.4 lists the corresponding structural parameters. From the line broadening of the (111) Ni peak at $2\theta \sim 44$ °, the mean crystallite size of the exsolved Ni particles of ~ 60 nm estimated using the Scherer equation[53], is in good agreement with TEM observation (Fig. 3).
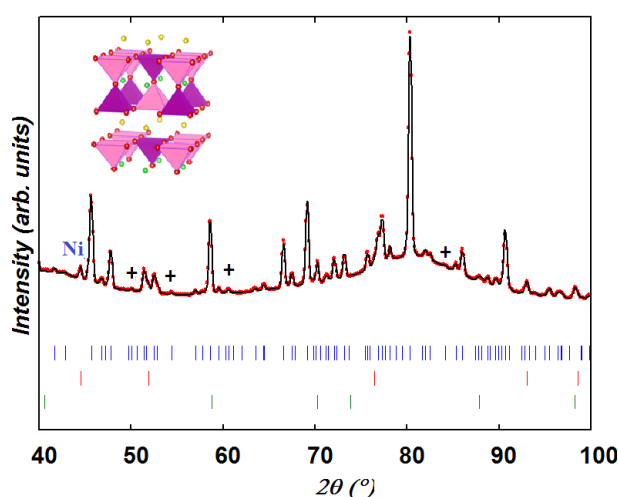
Fig. 9. Rietveld profile at $T \sim 60$ °C at the end of the heating/cooling cycle; (upper) PrBaMnO$_5$, (middle) Ni (bottom) MnO. R_p = 7.63 %, R_{wp} = 6.72 %, χ^2 = 5.55. Few peaks not indexed in $P4/mmm$ S.G. are labelled (+). The Mn^{3+}O$_5$/Mn^{2+}O$_5$ polyhedra are drawn in pink/purple.

Electrochemical measurements

To evaluate the catalytic activity towards H$_2$ oxidation, the electrochemical performance of PBMN symmetric cells was studied by electrochemical impedance spectroscopy (EIS) under 5% H$_2$/A flow in the temperature range 850-650 °C and compared to that of PrBaMn$_2$O$_5$ (PBM). The impedance diagrams can be fitted with the equivalent circuit consisting of two

resistance (R)-constant phase element (CPE) parallel circuits connected to an inductance (L) and a series resistance (R_s). The inductance, L, is primarily ascribed to the electrical wires and ranges between 0.5×10^{-6} H and 1.0×10^{-6} H for the present system in agreement with the literature data using a similar set-up[54]. The series resistance R_s is mainly correlated to the ohmic losses originating from the electrolyte. A conductivity of $\sim 2 \times 10^{-2}$ S cm^{-1} was calculated from the fitted R_s value of the data obtained at 800 °C and is in good agreement with the literature[55]. Fig. 10a presents the impedance results obtained for the two samples at 800 °C. In order to emphasize the anodic part of the impedance response, the diagrams are presented after subtraction of the L and R_s contributions. They consist of two elementary contributions.

a   b
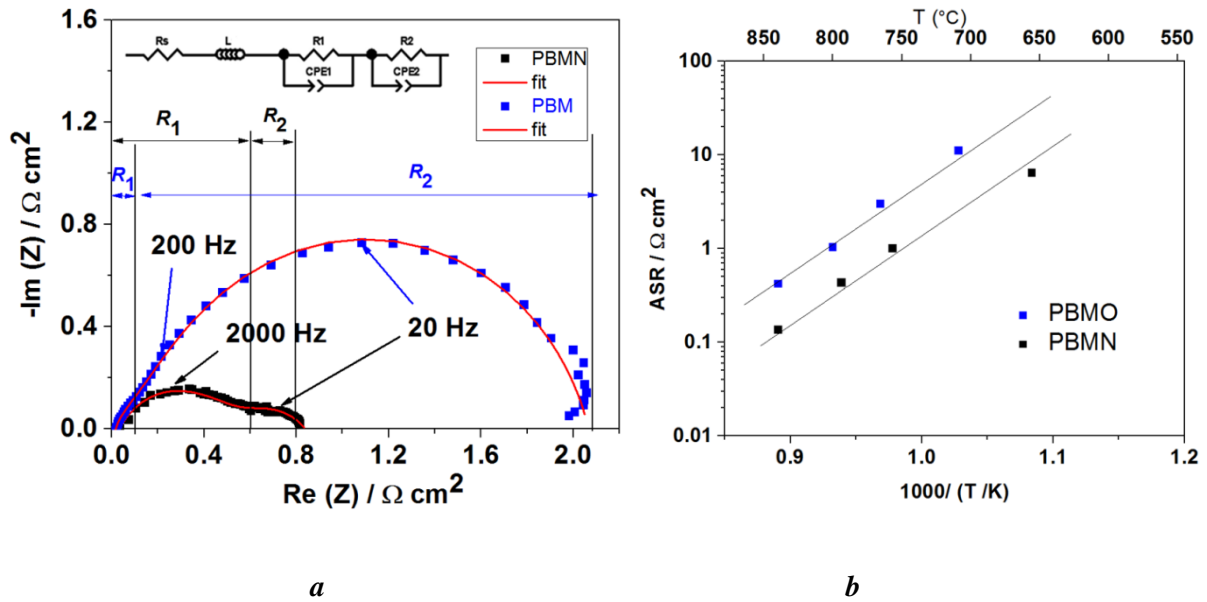
Fig. 10. Electrochemical performance for symmetric cells with PBMN and PBMO electrodes in 5 % H$_2$/Ar (a) Nyquist impedance diagrams at 800 °C at OCV (b) Arrhenius plot.

For PBMO, sample, the capacitances C_1 and C_2 associated to these processes are 0.95 mF cm^{-2} and 3.6 mF cm^{-2}, showing that the polarization resistance, R_p, ($Rp = \frac{R1+R2}{2}$) is only due to

mass transfer, such as adsorption of H_2, dissociation of H_2, and charge transfer- diffusion (O^{2-}) in the electrode [56]. On the contrary, for PBMN, the polarization resistance R_p is lower, with C_1 and C_2 capacitances of 2.5 $\mu F\ cm^{-2}$ and 17 $mF\ cm^{-2}$, respectively suggesting that in this case, only the low frequency contribution is related to the mass transfer phenomena. The decrease of mass transfer resistance reveals the promoted effect of Ni-exsolution on the catalytic activity for the oxidation of H_2 and the possibility of using PBMN as hydrogen electrode material for SOFC. The thermal variation of the polarization resistance, R_p, is shown in Fig. 10b. The R_p values of PBM are always larger than those of PBMN and decrease with increasing temperature with the same activation energy of 1.38 eV. At $T = 850\ °C$, R_p values for PBM and PBMN correspond to 0.43 and 0.135 $\Omega\ cm^2$, respectively.

PBMN anode shows similar performance to PBM electrodes doped with much larger amount of transition metals[37] and to PBM-YSZ composite electrodes ($R_p = 0.13\ \Omega\ cm^2$ at 850 °C)[57]. With further optimization of the electrode composition and thickness, interfaces, and microstructural and architectural design, the EIS performance can be largely improved as demonstrated for $La_{0.75}Sr_{0.25}Cr_{0.5}Mn_{0.5}O_{3-\delta}$ (LSCM) for which the polarization resistance decreased considerably when composite (LSCM-YSZ/CGO) and graded electrode were used [58,59].

Conclusion

The present work demonstrates that the introduction of a small amount of nickel into the $(PrBa)_{0.5}MnO_3$ perovkite produces a mixture of orthorhombic $Pr_{0.67}Ba_{0.33}Mn_{0.975}Ni_{0.025}O_3$ and hexagonal $BaMnO_{3-\delta}$ perovskite phases after annealing in air at 950 °C. High-Temperature NPD under wet hydrogen reveals exsolution of MnO phase at $T \geq 490\ °C$ and the detection of

a structural phase transition from *Ibmm* to *I4/mcm* then to cubic *Pm-3m* symmetry at *T* ~ 700 °C. In the 800-900 °C temperature range, further oxygen loss from both perovskites resulting in ~ 2.5 oxygen atoms/f.u. in both phases triggers the construction of a Ni-free double perovskite. During this process, the Ni^{2+} ions, present in the *A*-site disordered perovskite are pulled outside the structure and reduce to metal Ni particles. The fraction of the exsolved Ni particles evaluated at ~ 0.06 wt. % corresponds to the whole amount of nickel introduced and differs from the value of ~ 58 % previously reported[37]. These findings may provide new insights into the exsolution mechanism triggered by crystal reconstruction and implications for producing nanostructured materials. The Ni-exsolved layered perovskite presents better electrochemical performance than $PrBaMn_2O_5$ in hydrogen atmosphere which can be improved by optimizing electrode architecture (composition, thickness, sintering temperature).

Acknowledgements

References

(1)   Wachsman, E. D.; Marlowe, C. A.; Lee, K. T. *Energy & Environmental Science* **2012**, *5*, 5498.

(2)   Gorte, R. J.; Park, S.; Vohs, J. M.; Wang, C. *Advanced Materials* **2000**, *12*, 1465.

(3)   Brandon, N. P.; Skinner, S.; Steele, B. C. H. *Annual Review of Materials Research* **2003**, *33*, 183.

(4)   Wang, W.; Su, C.; Wu, Y.; Ran, R.; Shao, Z. *Chemical Reviews* **2013**, *113*, 8104.

(5)   Liu, M.; Lynch, M. E.; Blinn, K.; Alamgir, F. M.; Choi, Y. *Materials Today* **2011**, *14*, 534.

(6)   McIntosh, S.; Gorte, R. J. *Chemical Reviews* **2004**, *104*, 4845.

(7)   Choi, S.; Sengodan, S.; Park, S.; Ju, Y. W.; Kim, J.; Hyodo, J.; Jeong, H. Y.; Ishihara, T.; Shin, J.; Kim, G. *Journal of Materials Chemistry A* **2016**, *4*, 1747.

(8)   Tonus, F.; Bahout, M.; Dorcet, V.; Sharma, R. K.; Djurado, E.; Paofai, S.; Smith, R. I.; Skinner, S. J. *Journal of Materials Chemistry A* **2017**, *5*, 11078.

(9)   Tonus, F.; Bahout, M.; Dorcet, V.; Gauthier, G. H.; Paofai, S.; Smith, R. I.; Skinner, S. J. *Journal of Materials Chemistry A* **2016**, *4*, 11635.

(10)   Pineda, O. L.; Moreno, Z. L.; Roussel, P.; Świerczek, K.; Gauthier, G. H. *Solid State Ionics* **2016**, *288*, 61.

(11)   Sengodan, S.; Choi, S.; Jun, A.; Shin, T. H.; Ju, Y.-W.; Jeong, H. Y.; Shin, J.; Irvine, J. T. S.; Kim, G. *Nat Mater* **2015**, *14*, 205.

(12)   Kan, W. H.; Samson, A. J.; Thangadurai, V. *Journal of Materials Chemistry A* **2016**, *4*, 17913.

(13)   Thommy, L.; Joubert, O.; Hamon, J.; Caldes, M.-T. *International Journal of Hydrogen Energy* **2016**, *41*, 14207.

(14)   Hua, B.; Li, M.; Sun, Y.-F.; Li, J.-H.; Luo, J.-L. *ChemSusChem* **2017**, *10*, 3333.

(15)   Jiang, S. P. *Materials Science and Engineering: A* **2006**, *418*, 199.

(16)   Ishihara, T. *J. Korean Ceram. Soc* **2016**, *53*, 469.

(17)   Lou, X.; Liu, Z.; Wang, S.; Xiu, Y.; Wong, C. P.; Liu, M. *Journal of Power Sources* **2010**, *195*, 419.

(18)   Gong, Y.; Palacio, D.; Song, X.; Patel, R. L.; Liang, X.; Zhao, X.; Goodenough, J. B.; Huang, K. *Nano Letters* **2013**, *13*, 4340.

(19)   Tanaka, H.; Uenishi, M.; Taniguchi, M.; Tan, I.; Narita, K.; Kimura, M.; Kaneko, K.; Nishihata, Y.; Mizuki, J. i. *Catalysis Today* **2006**, *117*, 321.

(20)   Myung, J.-h.; Neagu, D.; Miller, D. N.; Irvine, J. T. S. *Nature* **2016**, *537*, 528.

(21)   Yang, G.; Zhou, W.; Liu, M.; Shao, Z. *ACS Applied Materials & Interfaces* **2016**, *8*, 35308.

(22)   Du, Z.; Zhao, H.; Yi, S.; Xia, Q.; Gong, Y.; Zhang, Y.; Cheng, X.; Li, Y.; Gu, L.; Świerczek, K. *ACS Nano* **2016**, *10*, 8660.

(23)   Cui, S.; Li, J.; Zhou, X.-W.; Wang, G.; Luo, J.-L.; T. Chuang, K.; Qiao, L.; Bai, Y. *Cobalt doped LaSrTiO3-δ as anode catalyst : Effect of Co nano-particles precipitation on SOFCs operating on H2S-containing hydrogen*, 2013; Vol. 1.

(24)   Liu, S.; Liu, Q.; Luo, J.-L. *ACS Catalysis* **2016**, *6*, 6219.

(25)   Jardiel, T.; Caldes, M. T.; Moser, F.; Hamon, J.; Gauthier, G.; Joubert, O. *Solid State Ionics* **2010**, *181*, 894.

(26)   Delahaye, T.; Jardiel, T.; Joubert, O.; Laucournet, R.; Gauthier, G.; Caldes, M. T. *Solid State Ionics* **2011**, *184*, 39.

(27)   Sun, Y.-F.; Li, J.-H.; Wang, M.-N.; Hua, B.; Li, J.; Luo, J.-L. *Journal of Materials Chemistry A* **2015**, *3*, 14625.

(28)   Sun, Y.-F.; Li, J.-H.; Cui, L.; Hua, B.; Cui, S.-H.; Li, J.; Luo, J.-L. *Nanoscale* **2015**, *7*, 11173.

(29)   Neagu, D.; Tsekouras, G.; Miller, D. N.; Ménard, H.; Irvine, J. T. S. *Nature Chemistry* **2013**, *5*, 916.

(30)   Gao, Y.; Chen, D.; Saccoccio, M.; Lu, Z.; Ciucci, F. *Nano Energy* **2016**, *27*, 499.

(31)   Ellouze, M.; Boujelben, W.; Cheikhrouhou, A.; Fuess, H.; Madar, R. *Solid State Communications* **2002**, *124*, 125.

(32)   Parras, M.; González-Calbet, J. M.; Alonso, J.; Vallet-Regí, M. *Journal of Solid State Chemistry* **1994**, *113*, 78.

(33)   Sengodan, S.; Ju, Y.-W.; Kwon, O.; Jun, A.; Jeong, H. Y.; Ishihara, T.; Shin, J.; Kim, G. *ACS Sustainable Chemistry & Engineering* **2017**, *5*, 9207.

(34)   Sun, Y.-F.; Zhang, Y.-Q.; Chen, J.; Li, J.-H.; Zhu, Y.-T.; Zeng, Y.-M.; Amirkhiz, B. S.; Li, J.; Hua, B.; Luo, J.-L. *Nano Letters* **2016**, *16*, 5303.

(35)   Madsen, B. D.; Kobsiriphat, W.; Wang, Y.; Marks, L. D.; Barnett, S. A. *Journal of Power Sources* **2007**, *166*, 64.

(36)   Arrive, C.; Delahaye, T.; Joubert, O.; Gauthier, G. *Journal of Power Sources* **2013**, *223*, 341.

(37)   Kwon, O.; Sengodan, S.; Kim, K.; Kim, G.; Jeong, H. Y.; Shin, J.; Ju, Y.-W.; Han, J. W.; Kim, G. *Nature Communications* **2017**, *8*, 15967.

(38)   Neagu, D.; Oh, T.-S.; Miller, D. N.; Ménard, H.; Bukhari, S. M.; Gamble, S. R.; Gorte, R. J.; Vohs, J. M.; Irvine, J. T. S. *Nature Communications* **2015**, *6*, 8120.

(39)   Hansen, T. C.; Henry, P. F.; Fischer, H. E.; Torregrossa, J.; Convert, P. *Measurement Science and Technology* **2008**, *19*, 034001.

(40)   Tonus, F.; Bahout, M.; Battle, P. D.; Hansen, T.; Henry, P. F.; Roisnel, T. *Journal of Materials Chemistry* **2010**, *20*, 4103.

(41)   Rietveld, H. M. *Journal of Applied Crystallography* **1969**, *2*, 65.

(42)   McCusker, L. B.; Von Dreele, R. B.; Cox, D. E.; Louër, D.; Scardi, P. *Journal of Applied Crystallography* **1999**, *32*, 36.

(43)   Rodríguez-Carvajal, J. *Physica B: Condensed Matter* **1993**, *192*, 55.

(44)   Berar, J.-F.; Baldinozzi, G. *Journal of Applied Crystallography* **1993**, *26*, 128.

(45)   Joo, S.; Kwon, O.; Kim, K.; Kim, S.; Kim, H.; Shin, J.; Jeong, H. Y.; Sengodan, S.; Han, J. W.; Kim, G. *Nature Communications* **2019**, *10*, 697.

(46)   Ricoul, F.; Subrenat, A.; Joubert, O.; Le Gal La Salle, A. *Journal of Solid State Electrochemistry* **2018**, *22*, 2789.

(47)   Trukhanov, S. V.; Khomchenko, V. A.; Lobanovski, L. S.; Bushinsky, M. V.; Karpinsky, D. V.; Fedotova, V. V.; Troyanchuk, I. O.; Trukhanov, A. V.; Stepin, S. G.; Szymczak, R.; Botez, C. E.; Adair, A. *Journal of Experimental and Theoretical Physics* **2006**, *103*, 398.

(48)   Sears, V. F. *Neutron News* **1992**, *3*.

(49)   Shannon, R. D. *Acta Crystallographica Section A* **1976**, *32*, 751.

(50)   Jirak, Z.; Pollert, E.; Andersen, A. F.; Grenier, J. C.; Hagenmuller, P. *European Journal of Solid State and Inorganic Chemistry* **1990**, *27*, 421.

(51)   Hcini, S.; Zemni, S.; Triki, A.; Rahmouni, H.; Boudard, M. *Journal of Alloys and Compounds* **2011**, *509*, 1394.

(52)   Kim, J. H.; Manthiram, A. *Electrochimica Acta* **2009**, *54*, 7551.

(53)   Patterson, A. L. *Physical Review* **1939**, *56*, 978.

(54)   Marrero-López, D.; Peña-Martínez, J.; Ruiz-Morales, J. C.; Gabás, M.; Núñez, P.; Aranda, M. A. G.; Ramos-Barrado, J. R. *Solid State Ionics* **2010**, *180*, 1672.

(55)   Ricoul, F.; Subrenat, A.; Joubert, O.; Le Gal La Salle, A. *International Journal of Hydrogen Energy* **2017**, *42*, 21215.

(56)   Fu, Q. X.; Tietz, F.; Stöver, D. *Journal of The Electrochemical Society* **2006**, *153*, D74.

(57)   Sun, Y.-F.; Zhang, Y.-Q.; Hua, B.; Behnamian, Y.; Li, J.; Cui, S.-H.; Li, J.-H.; Luo, J.-L. *Journal of Power Sources* **2016**, *301*, 237.

(58)   Jung, I.; Lee, D.; Lee, S. O.; Kim, D.; Kim, J.; Hyun, S.-H.; Moon, J. *Ceramics International* **2013**, *39*, 9753.

(59)   He, S.; Dai, H.; Cai, G.; Chen, H.; Guo, L. *Electrochimica Acta* **2015**, *152*, 155.